

**Title:** Minian: An open-source miniscope analysis pipeline

**Authors:** Zhe Dong<sup>1</sup>, William Mau<sup>1</sup>, Yu (Susie) Feng<sup>1</sup>, Zachary T. Pennington<sup>1</sup>, Lingxuan Chen<sup>1</sup>, Yosif Zaki<sup>1</sup>, Kanaka Rajan<sup>1</sup>, Tristan Shuman<sup>1</sup>, Daniel Aharoni<sup>\*2</sup>, Denise J. Cai<sup>\*1</sup>

\*Corresponding Authors

<sup>1</sup>Nash Family Department of Neuroscience, Icahn School of Medicine at Mount Sinai

<sup>2</sup>Department of Neurology, David Geffen School of Medicine, University of California

## Abstract

Miniature microscopes have gained considerable traction for *in vivo* calcium imaging in freely behaving animals. However, extracting calcium signals from raw videos is a computationally complex problem and remains a bottleneck for many researchers utilizing single-photon *in vivo* calcium imaging. Despite the existence of many powerful analysis packages designed to detect and extract calcium dynamics, most have either key parameters that are hard-coded or insufficient step-by-step guidance and validations to help the users choose the best parameters. This makes it difficult to know whether the output is reliable and meets the assumptions necessary for proper analysis. Moreover, large memory demand is often a constraint for setting up these pipelines since it limits the choice of hardware. Given these difficulties, there is a need for a low memory demand, user-friendly tool offering interactive visualizations of how altering parameters affects data output. Our open-source analysis pipeline, Minian (Miniscope Analysis), facilitates the transparency and accessibility of single-photon calcium imaging analysis, permitting users with little computational experience to extract the location of cells and their corresponding calcium traces and deconvolved neural activities. Minian contains interactive visualization tools for every step of the analysis, as well as detailed documentation and tips on parameter exploration. Furthermore, Minian has relatively small memory demands and can be run on a laptop, making it available to labs that do not have access to specialized computational hardware. Minian has been validated to reliably and robustly extract calcium events across different brain regions and from different cell types. In practice, Minian provides an open-source calcium imaging analysis pipeline with user-friendly interactive visualizations to explore parameters and validate results.

## Introduction

### *Overview of related works*

Open-source projects—hardware, software, training curricula—have changed science and enabled significant advances across multiple disciplines. Neuroscience, in particular, has benefitted tremendously from the open-source movement. Numerous open-source projects have emerged [1,2], including various types of behavioral apparatus facilitating the design of novel experiments [3,4,5,6], computational tools enabling the analysis of large scale datasets [7,8,9,10,11,12,13,14,15,16,17,18,19,20], and recording devices allowing access to large populations of neurons in the brain [21,22,23,24,25,26,27,28,29,30]. Miniature microscopy has been an area of particular importance for the open-source movement in neuroscience. To increase the usability, accessibility, and transparency of this remarkable technology originally developed by Schnitzer and colleagues [31,32], a number of labs innovated on top of the original versions with open-source versions [25,26,27,28,29,30]. The UCLA Miniscope project, a miniature head-mounted microscope for *in vivo* calcium imaging in freely behaving animals, is one such project [21]. The UCLA Miniscopes project increased the tool's impact by creating versions that are user-friendly and accessible to a large number of users [33].

With the increasing popularity of miniature microscopes, there is a growing need for analysis pipelines that can reliably extract neuronal activities from recording data. To address this need, numerous algorithms have been developed and made available to the neuroscience community. The principal component analysis or independent component analysis (PCA-ICA)-based

approach [12], and region-of-interest (ROI)-based approach [34] were among the earliest algorithms that reliably detected the locations of neurons and extract their overall activities across pixels. However, one of the limitations of these approaches is that activities from cells that are spatially overlapping cannot be demixed. A subsequent constrained non-negative matrix factorization (CNMF) approach was shown to reliably extract neuronal activity from both two-photon and single-photon calcium imaging data [35], and demix the activities of overlapping cells. The CNMF algorithm models the video as a product of a ‘spatial’ matrix containing detected neuronal footprints (locations of cells) and a ‘temporal’ matrix containing the temporal calcium traces of each detected cell. This approach is particularly effective at addressing crosstalk between neurons, which is of particular concern in single-photon imaging, where the fluorescence from overlapping or nearby cells contaminate each other. Moreover, by deconvolving calcium traces, the CNMF algorithm enables a closer exploration of the underlying activity of interest, action potentials [18,36]. Originally developed for two-photon data, the CNMF algorithm did not include an explicit model of the out-of-focus fluorescence which is often present in single-photon miniature microscope recordings. This issue was addressed via the CNMF-E algorithm [10], where a ring-model is used as a background term to account for out-of-focus fluorescence. Later, an open-source python pipeline for calcium imaging analysis, CalmAn, was published, which included both the CNMF and CNMF-E algorithms, as well as many other functionalities [15]. The latest development in analysis pipelines for *in vivo* miniature microscope data is MIN1PIPE [11], where a morphological operation is used to remove background fluorescence during pre-processing of the data, and a seed-based approach is used for initialization of the CNMF algorithm. Other approaches have also been used to extract signals from calcium imaging data including an online approach [19],  $\ell_0$ -penalization approach to infer spikes [13,20], and source detection using neural networks [14].

The open sharing of the algorithms necessary for the computation of neural activity has been exceptionally important for the field. However, implementation of these tools can be complex as many algorithms have numerous free parameters (those that must be set by the user) that can influence the outcomes, without clear guidance on how these parameters should be set or to what extent they affect results. Moreover, there is a lack of ground-truth data for *in vivo* miniature microscope imaging, making it hard to validate algorithms and/or parameters. Together, these obstacles make it challenging for neuroscience labs to adopt the analysis pipelines, since it is difficult for researchers to adjust parameters to fit their data, or to trust the output of the pipeline for downstream analysis. Thus, the next challenge in open-source analysis pipelines for calcium imaging is to make the analysis tools more user-friendly and underlying algorithms more accessible to neuroscience labs so that researchers can more easily understand the pipeline and interpret the results.

### *Contributions of Minian*

To increase the accessibility of the mathematical algorithms, transparency into how altering parameters alters the data output, and usability for researchers with limited computational resources and experience, we developed Minian, an open-source analysis pipeline for single-photon calcium imaging data inspired by previously published algorithms. We based Minian on the CNMF algorithm [15,35], but also leverage methods from other pipelines, including those originally published by Cai et al. [34] and MIN1PIPE [11]. To enhance compatibility with different types of hardware, especially laptops or personal desktop computers, we implemented an

approach that supports parallel and out-of-core computation (*i.e.* computation on data that are too large to fit a computer's memory). We then developed interactive visualizations for every step in Minian and integrated these steps into annotated Jupyter Notebooks as an interface for the pipeline. We have included detailed notes and discussions on how to adjust the parameters from within the notebook and have included all free parameters in the code for additional flexibility. The interactive visualizations will help users to intuitively understand and visually inspect the effect of each parameter, which we hope will facilitate more usability, transparency, and reliability in calcium imaging analysis.

Minian contributes to three key aspects of calcium image data analysis:

1. **Visualization.** For each step in the pipeline, Minian provides visualizations of inputs and results. Thus, users can proceed step-by-step with an understanding of how the data are transformed and processed. In addition, all visualizations are interactive and support simultaneous visualization of the results obtained with different parameters. This feature provides users with knowledge about which parameter values should be used to achieve the best outcomes and whether the results appear accurate. Hence, the visualizations also facilitate parameter exploration for each step, which is especially valuable when analyzing data from heterogeneous origins that may vary by brain region, cell type, species, and the extent of viral transfection.
2. **Memory demand.** One of the most significant barriers in adopting calcium imaging pipelines is the memory demand of algorithms. The recorded imaging data usually take up tens of gigabytes of space when converted to floating-point datatypes and often cannot fit into the RAM of standard computers without spatially and/or temporally down-sampling. CalmAn addresses this issue by splitting the data into overlapping patches of pixels, processing each patch independently, and merging the results together. This enables out-of-core computation since at any given time only subsets of data are needed and loaded into memory. In Minian, we extend this concept further by flexibly splitting the data either spatially (split into patches of pixels) or temporally (split into chunks of frames). In this way, we avoid the need to merge the results based on overlapping parts. The result is a pipeline that supports out-of-core computation at each step, which gives nearly constant memory demand with respect to input data size. Minian can process more than 20min of recording with 8GB of memory, which makes Minian suitable to be deployed on modern personal laptops.
3. **Accessibility.** Minian is an open-source Python package. In addition to the codebase, Minian distributes several Jupyter Notebooks that integrate explanatory text with code and interactive visualizations of results. For each step in the notebook, detailed instructions, as well as intuition about the underlying mathematical formulation are provided, along with the actual code, which can be directly executed from within the notebook. Upon running a piece of code, visualizations appear directly below that code in the notebook. In this way, the notebooks serve as a complement to traditional API documentations of each function. In addition, users can easily rearrange and modify the pipeline notebook to suit their needs without diving into the codebase and modifying the underlying functions. The notebooks distributed by Minian can simultaneously function as a user guide, template, and production tool. We believe the inclusion of these notebooks, in combination with Minian's

other unique features, can increase understanding of the underlying functioning of the algorithms and greatly improve the accessibility of miniature microscopy analysis pipelines.

### *Paper organization*

The paper is organized as follows: Since Minian's major contribution is usability and accessibility, we first present the detailed steps in the analysis pipeline in Materials and methods section. Following a step-by-step description of the algorithms Minian adopted from existing works, we present novel visualizations of the results, as well as how users can utilize these visualizations. In the Results section, we benchmark Minian across two brain regions and show that spatial footprints and the temporal activity of cells can be reliably extracted. We also show that the cells extracted by Minian in hippocampal CA1 exhibit stable spatial firing properties consistent with the existing literature.

## **Materials and methods**

Here, we present a detailed description of Minian. We begin with an overview of the Minian pipeline. Then, we provide an explanation of each step, along with the visualizations. Lastly, we provide information regarding hardware and dependencies.

### *Overview of Minian*

Minian comprises five major stages, as shown in Figure 1. Raw videos are first passed into a pre-processing stage. During pre-processing, the background caused by vignetting (in which the central portion of the field of view is brighter) is corrected by subtracting a minimum projection of the movie across time. Sensor noise, evident as granular specks, is then corrected with a median filter. Finally, background fluorescence is corrected by the morphological process introduced in MIN1PIPE [11]. The pre-processed video is then motion-corrected with a standard template-matching algorithm based on cross-correlation between each frame and a reference frame [37]. The motion-corrected and pre-processed video then serves as the input to initialization and CNMF algorithms. The seed-based initialization procedure looks for local maxima in max projections of different subsets of frames and then generates an over-complete set of seeds, which are candidate pixels for detected neurons. Because this process is likely to produce many false positives, seeds are then further refined based on various metrics, including the amplitude of temporal fluctuations and the signal-to-noise ratio of temporal signals. The seeds are transformed into an initial estimation of cells' spatial footprints based on the correlation of neighboring pixels with each seed pixel, and the initial temporal traces are in turn estimated based on the weighted temporal signal of spatial footprints. Finally, the processed video, initial spatial matrix, and temporal matrix are fed into the CNMF algorithm. The CNMF algorithm first refines the spatial footprints of the cells (spatial update). The algorithm then denoises the temporal traces of each cell while simultaneously deconvolving the calcium trace into estimated 'spikes' (temporal update). CNMF spatial and temporal updates are performed iteratively and can be repeated until a satisfactory result is reached through visual inspection. Typically, this takes two cycles of spatial, followed by temporal, updates. Minian also includes a demo dataset which allows the user to run and test the pipeline comprised of the pre-made Jupyter Notebook immediately after installation.

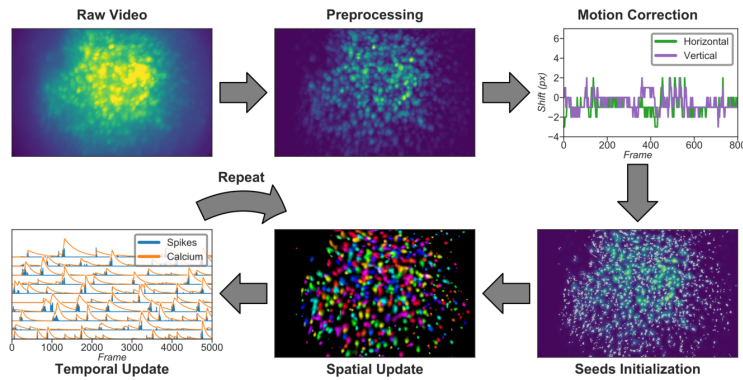


**Figure 1: Overview of the analysis pipeline.** The analysis is divided into five stages: Pre-processing, where sensor noise and background fluorescence from scattered light are removed; Motion-correction, where rigid motion of the brain is corrected; Seeds-initialization, where the initial spatial and temporal matrices for later steps are generated from a seed-based approach; Spatial update, where the spatial footprints of cells are further refined; Temporal update, where the temporal signals of cells are further refined. The last two steps of the pipeline are iterative and can be repeated multiple times until a satisfactory result is reached.

### Pre-processing

#### Loading data and down-sampling

Currently Minian supports .avi movies, the default output from the UCLA Miniscopes, and .tif stacks, the default output from Inscopix miniscopes. This functionality can be easily extended to support more formats if desired. Users are required to organize their data so that each recording session is contained in a single folder. Because Minian can extract relevant metadata from folder nomenclature (e.g., animal name, group, date), we suggest organizing the video folders based upon animal and other experiment-related groupings to facilitate the incorporation of metadata into Minian output files.

Minian supports down-sampling on any of the three video dimensions (height, width, and frames). Two down-sampling strategies are currently implemented: either sub-setting data on a regular interval or calculating a mean for each interval. At this stage, users are required to specify (1) the path to their data, (2) a pattern of file names to match all the videos to be processed (e.g., all files containing 'msCam', a typical pattern resulting from Miniscope recordings), (3) a Python dictionary specifying whether and how metadata should be pulled from folder names, (4) another Python dictionary specifying whether and on which dimension down-sampling should be carried out, and (5) the down-sampling strategy, if desired.

Once specified, the data can be immediately visualized through an interactive viewer, as shown in Figure 2. Along with a player to visualize every frame in the video, the viewer also plots summary values such as mean, maximum, or minimum fluorescence values across time. This helps users to check their input data and potentially exclude any artifacts caused by technical faults during experiments (e.g., dropped frames). Users can further subset data to exclude specified frames, if necessary. Finally, restricting the analysis to a certain sub-region of the field of view during specific steps could be beneficial. For example, if the video contains anchoring

artifacts resulting from dirt on the lenses, it is often better to avoid such regions during motion correction. To facilitate this, the viewer provides a feature where users can draw an arbitrary box within the field of view and have it recorded as a mask. This mask can be passed into later motion correction steps to avoid the biases resulting from the artifacts.

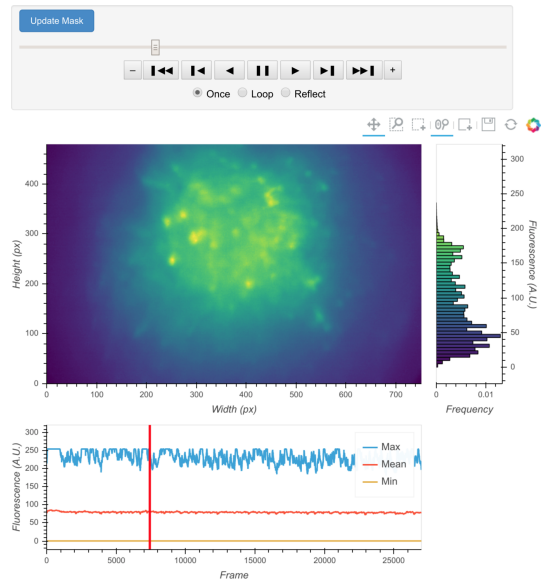


**Figure 2: Interactive visualization of raw input video.** One frame is shown in the central panel of the visualization which can be interactively updated with the player toolbar on the top. A histogram of fluorescence intensity of the current frame is shown on the right and will update in response to zooming in on the central frame. A line plot of summary values across time is shown on the bottom. Here the maximum, mean, and minimum fluorescence values are plotted. These summaries are useful in checking whether there are unexpected artifacts or gaps in the recording. Finally, the user can draw an arbitrary box in the central frame, and the position of this boxed region can be recorded and used as a mask during later steps. For example, during motion correction a sub-region of the data containing a stable landmark might provide better information on the motion.

#### Vignetting correction

Single-photon miniature microscope data often suffer from a vignetting effect in which the central portion of the field of view appears brighter than the periphery. Vignetting is deleterious to subsequent processing steps and should be removed. We find that the effect can be easily extracted by taking the minimum fluorescence value across time for each pixel and subtracting this value from each frame, pixel-wise. One of the additional benefits of subtracting the minimum is that it preserves the raw video's linear scale.

The result of this step can be visualized with the same video viewer used in the previous step. In addition to visualizing a single video, the viewer can also show multiple videos side-by-side (e.g., the original video and the processed video), as shown in Figure 3. The operation/visualization is carried out 'on-the-fly' upon request for each frame, and users do not have to wait for the operation to finish on the whole video to view the results.

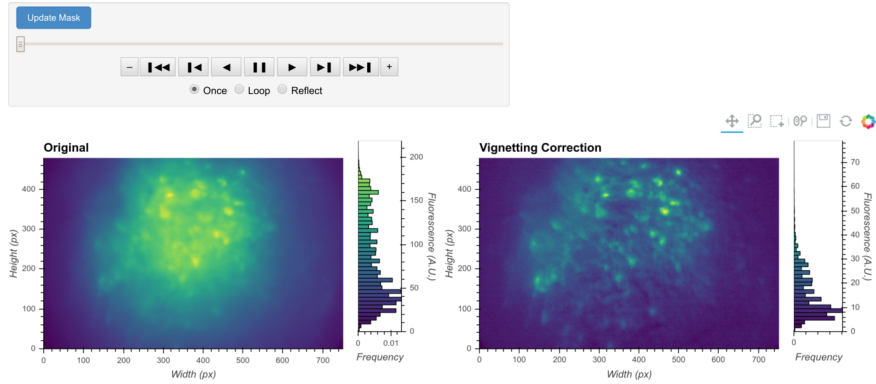


**Figure 3: General visualization of pre-processing.** The same visualization of input video can be used to visualize the whole video before and after specific pre-processing steps side-by-side. The effect of vignetting correction is visualized here. The image and accompanying histogram on the left side show the original data; the data after vignetting correction are shown on the right side. Any frame of the data can be selected with the player toolbar and histograms are responsive to all updates in the image.

### Denoising

Next, we correct for salt-and-pepper noise on each frame, which usually results from electronic pixel noise. By default, we pass each frame through a median filter, which is generally considered particularly effective at eliminating this type of noise, though other smoothing filters like Gaussian filters and anisotropic filters can also be implemented. The critical parameter here is the window size of the median filter. A window size that is too small will make the filter ineffective at correcting outliers, while a window size that is too large will remove finer gradient and edges that are much smaller than the window size, and can result in a failure to distinguish between adjacent cells.

The effect of the window size can be checked with an interactive visualization tool used across the pre-processing stage, as shown in Figure 4. Additionally, here we show an example of the effect of window size on the resulting data in Figure 5. Users should see significantly reduced amount of salt-and-pepper noise in the images, which should be made more obvious by the contour plots. At the same time, users should keep the window size below the extent where over-smoothing occurs. As a heuristic, the average cell radius in pixel units works well, since a window of the same size as an average cell is unlikely to blend different cells together, while still being able to adequately smooth the image.

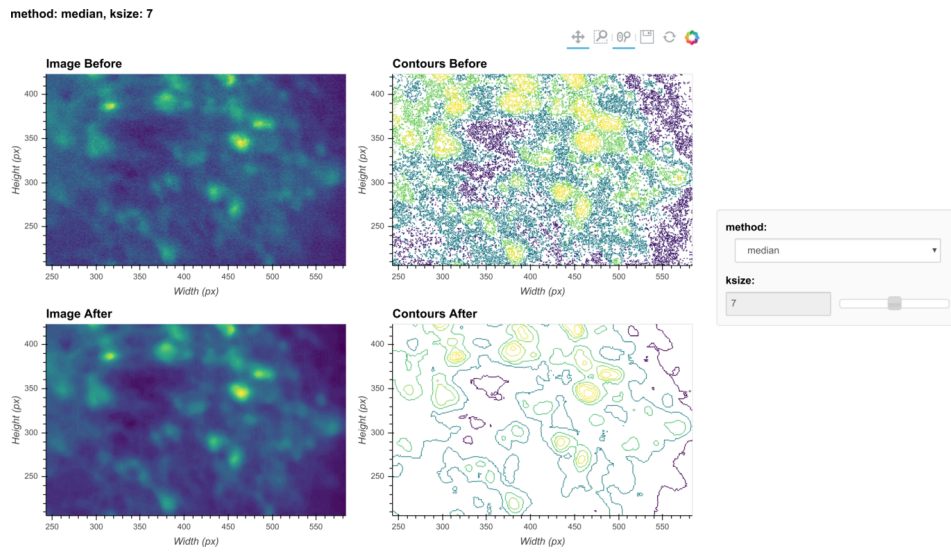


**Figure 4: Visualization of denoising.** Here, a single frame from the data is passed through the background removal and both the image and a contour plot are shown for the frame before and after the process. The contour plots show the iso-contour of 5 intensity levels spaced linearly across the full intensity range of the corresponding image. The plots are interactive and responsive to the slider of the window size on the right, thus the effect of different window sizes for denoising can be visualized.

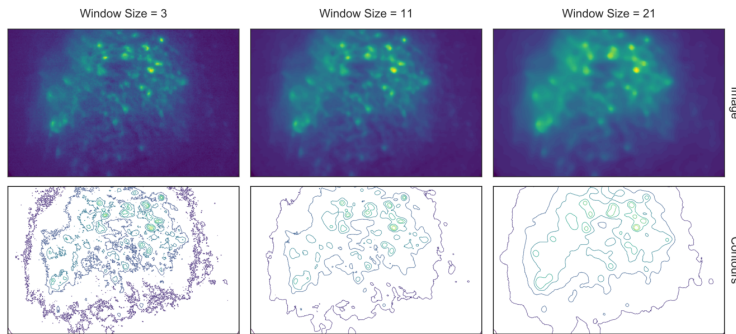


**Figure 5: Effect of window size on denoising.** One example frame is chosen from the data, and the resulting images (top row) and contour plots (bottom row) are shown to demonstrate the effect of window size on denoising. Here, a window size of 11 (middle column) is appropriate while both smaller and larger window sizes result in artifacts.

#### Morphological background removal

Next, we remove any remaining background presumably caused by out-of-focus and tissue fluorescence. To accomplish this, we estimate the background using a morphological opening process first introduced for calcium imaging analysis in MIN1PIPE [11], which acts as a size filter that removes cell bodies. The morphological opening is composed of two stages: erosion followed by dilation. In morphological erosion the image is passed through a filter where each pixel will be substituted by the minimum value within the filter window. The effect of this process is that any bright ‘feature’ that is smaller than the filter window will be ‘eroded’ away. Then the

dilation process accomplishes the reverse by substituting each pixel with the maximum value in the window, which ‘dilates’ small bright features to the extent of the filter window size. The combined effect of these two stages is that any bright ‘feature’ that is smaller than the filter window is removed from the image. If we choose the window size to match the expected cell diameter, performing a morphological opening will likely remove cells and provide a good estimation of background. Hence, each frame is passed through the morphological opening operation and the resulting image is subtracted from the original frame.

Although the window size parameter for the morphological opening can be pre-determined by the expected cell diameter, it is helpful to visually inspect the effect of morphological background removal. The effect of different window sizes can be visualized with the same tool used in denoising, as shown in Figure 6. Additionally, here we show an example of the effect of window size on the resulting data in Figure 7. In this case, a window size of 20 pixels is considered appropriate because the resulting cells are appropriately sized and sharply defined. In contrast, a smaller window results in limiting both the size and intensity of the cells. On the other hand, residual out-of-focus fluorescence becomes visible when the window size is set too large.

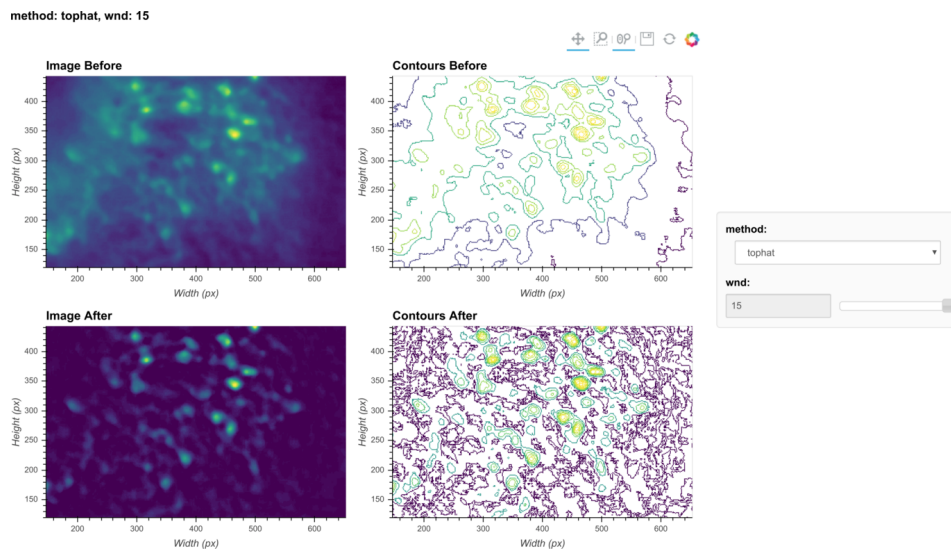


**Figure 6: Visualization of background removal.** Here, a single frame from the data is passed through background removal and both the image and a contour plot are shown for the frame before and after the process. The plots are interactive and responsive to the slider of the window size on the right, thus the effect of different window sizes for background removal can be visualized.

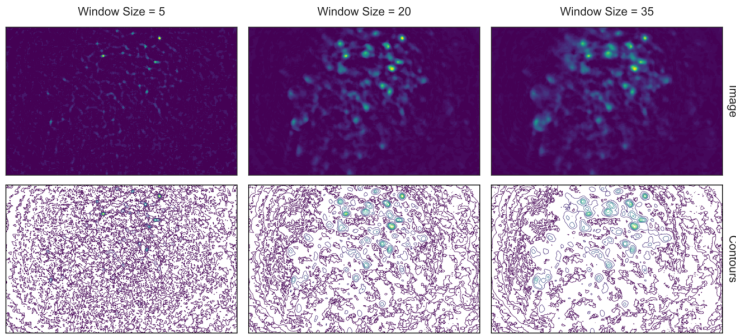


**Figure 7: Effect of window size on background removal.** One example frame is chosen from the data, and the resulting images (top row) and contour plots (bottom row) are shown to demonstrate the effect of window size on background removal. The contour plots show the iso-contour of 5 intensity levels spaced linearly across the full intensity range of the corresponding image. Here a window size of 20 pixels (middle column) is appropriate while both smaller and larger window sizes produce unsatisfactory results: a window size too small (left column) artificially limits the size of cells, and a window size too large (right column) does not remove the background effectively.

#### Motion correction

##### Estimate and apply translational shifts

We use a standard template-matching algorithm based on cross-correlation to estimate and correct for translational shifts [37]. In practice, we found that this approach is sufficient to correct for motion artifacts that could have a significant impact on the final outcome. Briefly, for a range of possible shifts, a cross-correlation between each frame and a template frame is calculated. The shift producing the largest cross-correlation is estimated to reflect the degree of movement from the template and is corrected by applying a shift to the frame in that direction. To properly handle border effects produced by cross-correlations with different degrees of shift, the template should be trimmed so that it is smaller than each frame. The amount of trimming in turn determines the maximal shift. In practice, the maximal shift can be set liberally, estimating the largest possible shift, since there is little drawback to setting this number large, as long as there is enough information left in the trimmed template for it to be correctly registered with each frame. Moreover, if the user would like to take advantage of anatomical landmarks (such as blood vessels) within the field of view and would like to implement motion correction before all of the background subtraction steps have been performed, the pipeline can be easily modified to do so. However, we recommend that initial smoothing of the image be performed first. After the estimation of shifts, the shift in each direction is plotted across time and visualization of the data before and after motion correction is displayed in Minian (see Figure 2, top right).

### *Seed initialization*

#### Generation of an over-complete set of seeds

The CNMF algorithm is a powerful approach to extract cells' spatial structure and corresponding temporal activity. However, the algorithm requires an initial estimate of cell locations/activity, which it then refines. We use a seed-based approach introduced in MIN1PIPE [11] to initialize spatial and temporal matrices for CNMF. The first step is to generate an over-complete set of seeds, representing the potential centroids of cells. We iteratively select a subset of frames, compute a maximum projection for these frames, and find the local maxima on the projections. This workflow is repeated multiple times and we take the union of all local maxima across repetitions to obtain an over-complete set of seeds. In this way, we avoid missing cells that only fire in short periods of time that might be masked by taking a maximum projection across the whole video.

During seed initialization, the first critical parameter is the spatial window for defining local maxima. Intuitively, this should be the expected diameter of cells. The other critical parameter is an intensity threshold for a local maximum to be considered a seed. Since the spatial window for local maxima is small relative to the field of view, a significant number of local maxima are usually false positives and do not actually reflect the location of cells. Thresholding the fluorescence intensity provides a simple way to filter out false local maxima, and usually a very low value is enough to produce satisfactory results. We have found a value of 3 usually works well (recall that the range of fluorescence intensity is usually 0-255 for unsigned 8-bit data). An alternative strategy to thresholding the intensity is to model the distribution of fluorescence fluctuations and keep the seeds with relatively higher fluctuations. This process is described in Seeds refinement with a Gaussian-Mixture-Model, and is accessible if the user prefers explicit modeling over thresholding.

Finally, the temporal sampling of frames for the maximum projections also impacts the result. We provide two implementations here: either taking a rolling window of frames across time, or randomly sampling frames for a user-defined number of iterations. For the rolling window approach, users can specify a temporal window size (the number of successive frames for each subset) and a step size (the interval between the start of subsets). For the random approach, users can specify the number of frames in each subset and the total number of repetitions. We use the rolling window approach as the default.

The resulting seeds are visualized on top of a maximum projection image (plot not shown). Although the spatial window size of local maxima can be pre-determined, the parameters for either the rolling window or random sampling of frames are hard to estimate intuitively. We provide default parameters that generally provide robust results. However, the user is also free to vary these parameters to obtain reasonable seeds. As long as the resulting seeds are not too dense (populating almost every pixel) or too sparse (missing cells that are visible in the max projection), subsequent steps can be performed efficiently and are fairly tolerable to the specific ways the seeds are initialized.

### Refinement with peak-to-noise ratio

Next, we refine the seeds by looking at what we call the peak-to-noise ratio of the temporal traces and discard seeds with low peak-to-noise ratios. To compute this ratio, we first separate the noise from the presumed real signal. Calcium dynamics are mainly composed of low frequency fluctuations (from the slow kinetics of the calcium fluctuations) while noise is composed of higher frequency fluctuations. Thus, to separate the noise from the calcium dynamics we pass the fluorescence time trace of each seed through a low-pass and a high-pass filter to obtain the ‘signal’ and ‘noise’ of each seed. We then compute the difference between the maximum and minimum values (or peak-to-peak values) for both ‘signal’ and ‘noise’, and the ratio between the two difference values defines the peak-to-noise ratio. Finally, we filter out seeds whose peak-to-noise value falls below a user-defined threshold.

The first critical parameter here is the cut-off frequency that separates ‘signal’ from ‘noise’. This parameter is also important for subsequent steps when implementing the CNMF algorithm. We provide a visualization tool, shown in Figure 8, to help users determine cut-off frequency. In the visualization, 6 seeds are randomly selected, and their corresponding ‘signal’ and ‘noise’ traces are plotted. The user is then able to use a dynamic slider on the right side of the plots to adjust the cut-off frequency and view the results. The goal is to select a frequency that best separates signal from noise. A cut-off frequency that is too low will leave true calcium dynamics absorbed in ‘noise’ (left panel in Figure 9), while a frequency that is too high will let ‘noise’ bleed into ‘signal’ (right panel in Figure 9). A suitable frequency is therefore the one where the ‘signal’ captures all of the characteristics of the calcium indicator dynamics (i.e., large, fast rise, and slow decay), while the ‘noise’ trace remains relatively uniform across time (middle panel in Figure 9). The interactive plots make this easy to visualize. We also provide an example in Figure 9 to show how cut-off frequency influences the separation of ‘signal’ from ‘noise’. The second parameter is the threshold of peak-to-noise ratio value. In practice, we have found a threshold of 1 works well in most cases. An additional advantage of using 1 is that it reflects the intuitive interpretation that fluctuations in a real ‘signal’ should be larger than fluctuations in ‘noise’.

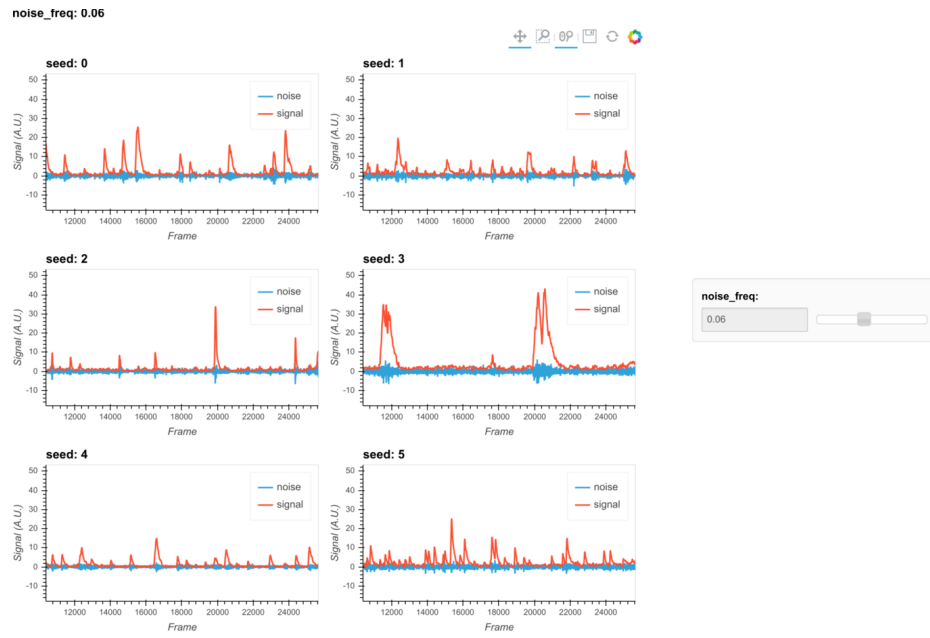


**Figure 8: Visualization of noise frequency cut-off.** The cut-off frequency for noise is one of the critical parameters in the pipeline that affects both the seed initialization process and CNMF's temporal update steps. Here we help the user determine that parameter by plotting temporal traces from six example seeds. In each plot the raw signal is passed through a high-pass and low-pass filter at the chosen frequency, and the resulting signals are plotted separately as “noise” and “signal”. The plots are responsive to the chosen frequency controlled by the slider on the right. In this way, the user can visually inspect whether the chosen frequency can effectively filter out high frequency noise without deforming the calcium signal.

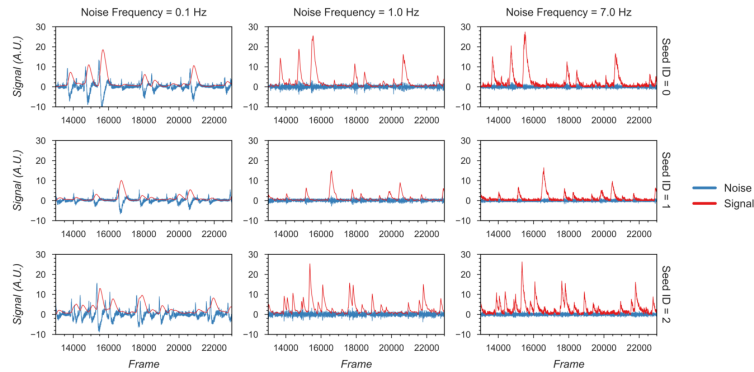


**Figure 9: Example of filtered traces with different frequency cut-offs.** Here the temporal dynamics of three example seeds are chosen, and the low-pass and high-pass filtered traces with different frequency cut-offs are shown. The low-pass filtered trace corresponds to ‘signal’, while the high-pass filtered trace corresponds to ‘noise’. Here a 1 Hz cut-off frequency is considered appropriate, since calcium dynamics and random noise are cleanly separated. A cut-off frequency smaller than 1 Hz left the calcium dynamics in the ‘noise’ trace, while a cut-off frequency larger than 1 Hz let random noise bleed into the ‘signal’ trace (i.e., high frequency fluctuations are presented in periods where the cells seem to be inactive).

## Refinement with Kolmogorov-Smirnov tests

Finally, we refine the seeds with a Kolmogorov-Smirnov test. The Kolmogorov-Smirnov test assesses the equality of two distributions and can be used to check whether the fluctuation of values for each seed is non-normally distributed, as would be expected of a real cell. In theory, the distribution of fluorescence values of a cell should be a mixture of two Gaussian distributions: one with low mean value corresponding to when the cell is silent, and the other with higher mean value corresponding to when the cell is active. Therefore, seeds corresponding to cells should be non-normally distributed. We use a default significance threshold of 0.05. In some cases, this might be too conservative or too liberal. Users can tweak this threshold or skip this step altogether depending on the resulting seeds.

## Merge seeds

There will usually be multiple seeds for a single cell and it is best to merge them whenever possible. We implement two criteria for merging seeds: first, the distance between the seeds must be below a given threshold, and second, the correlation coefficient of the temporal traces between seeds must be higher than a given threshold. To avoid bias in the correlation due to noise, we implement a smoothing operation on the traces before calculating the correlation. The critical parameters are the distance threshold, the correlation threshold, and the cut-off frequency for the smoothing operation. While the distance threshold is arbitrary and should be explored, often the average radius of cells provides a good starting point. The cut-off frequency should be the same as that used during the peak-to-noise-ratio refinement described above, and the correlation should be relatively high (we typically use 0.8, but this can be refined by the user). The resulting merged seeds can be visualized on the max projection. Since the main purpose of this step is to alleviate computation demands for downstream steps, it is fine to have multiple seeds for a single visually distinct cell. However, users should make sure each of the visually distinct cells still has at least one corresponding seed after the merge.

## Initialize spatial and temporal matrices from seeds

The last step before implementing CNMF is to initialize the spatial and temporal matrices for the CNMF algorithm from the seeds. The spatial matrix has one dimension representing each pixel and the other representing each putative cell, with its values representing the spatial footprint for each cell at each pixel location (in other words, each pixel has a weight on each cell). The temporal matrix has one dimension representing time and the other representing each cell, with its values representing the temporal fluorescence value of each cell on each frame. We assume each seed is the center of a potential cell, and we first calculate the spatial footprint for each cell by taking the cosine similarity between the temporal trace of a seed and the pixels surrounding that seed. In other words, we generate the weights in the spatial footprint by computing how similar the temporal activities of each seed are to the surrounding pixels. Then, we generate the temporal activities for each potential cell by taking the input video and weighting the contribution of each pixel to the cell's temporal trace by the spatial footprint of the cell. The final products are a spatial matrix and a temporal matrix.

Besides the two matrices representing neuronal signals, there are two additional terms in the CNMF model that account for background fluorescence modeled as a spatial footprint for the

background and a temporal trace of background activity. To estimate these terms, we subtract the dot product of our spatial and temporal matrices, which represent cellular activities, from the input data. We take the mean projection of this remainder across time as an estimation of the spatial footprint of the background, and we take the mean fluorescence for each frame as the temporal trace of the background.

Users can tweak two parameters to improve the outcome and performance of this step: a threshold for cosine similarity and a spatial window identifying pixels on which to perform this computation. To keep the resulting spatial matrix sparse and keep irrelevant pixels from influencing the temporal traces of cells, we set a threshold for the cosine similarity of temporal traces compared to the seed, where pixels whose similarity value falls below this threshold will be set to zero in the spatial footprint of the cell. Cosine similarity is, in essence, a correlation (the scale is 0-1) and thresholds of 0.5 and higher work well in practice. Computing many pairwise similarity measurements is computationally expensive, and it is unnecessary to compute the similarities between pixels that are far apart because they are unlikely to have originated from the same cell. We therefore set a window size to limit the number of pixel pairs to be considered. This size should be set large enough so that it does not limit the size of spatial footprints, but not unnecessarily large to the extent where it will impact performance. In practice, a window size equal to the maximum expected cell diameter is reasonable.

## CNMF

### Estimate spatial noise

CNMF requires that we first estimate the spatial noise over time for each pixel in the input video. The spatial noise of each pixel is simply the power of the high frequency signals in each pixel. The critical parameter here is again the cut-off frequency for ‘noise’, and users should employ the visualization tools as described above during peak-to-noise ratio refinement to determine this frequency (see Refinement with peak-to-noise ratio).

### Spatial update

Next, we proceed to the spatial update of the CNMF algorithm. The original paper describing this algorithm [35] contains a detailed theoretical derivation of the model. Here, we provide only a conceptual overview of the process so that users can understand the effect of each parameter. The CNMF framework models the input video to be the product of the spatial and temporal matrices representing signals contributed by real cells, a background term, and random noise. In equation form, this is  $\mathbf{Y} = \mathbf{AC} + \mathbf{B} + \mathbf{E}$ , where  $\mathbf{Y}$  represents the input video,  $\mathbf{A}$  represents the spatial matrix containing the spatial footprints for all putative cells,  $\mathbf{C}$  represents the temporal matrix containing the calcium dynamics for all putative cells,  $\mathbf{B}$  represents the spatial-temporal fluctuation of background, and  $\mathbf{E}$  represents error or noise. Since the full problem of finding proper  $\mathbf{A}$  and  $\mathbf{C}$  matrices is hard (non-convex), we break down the full process into spatial update and temporal update steps, where iterative updates of  $\mathbf{A}$  and  $\mathbf{C}$  are carried out, respectively. Each iteration will improve on previous results and eventually converge on the best estimation.

During the spatial update, given an estimation of the temporal matrix and the background term, we seek to update the spatial matrix so that it best fits the input data, along with the corresponding temporal traces. To do so, we first subtract the background term from the input data so that the remainder is composed only of signals from cells and noise. Then, for each pixel, the algorithm attempts to find the weights for each cell's spatial footprint that best reproduces the input data ( $\mathbf{Y}$ ) with the constraint that individual pixels should not weigh on too many cells (controlled through what is called a sparseness penalty). To reduce computational demand, we do this for each pixel independently and in parallel to improve performance, while retaining the 'demixing' power of the CNMF algorithm by updating the weights for all cells simultaneously. In the optimization process, the function to be minimized contains both a squared error term to assess error, and an  $\ell_1$ -norm term to promote sparsity [15].

In other CNMF implementations, the estimated spatial noise is used to determine the scaling of the  $\ell_1$ -norm term in the target function and control the balance between error and sparsity of the result. However, in practice we find that it does not always give the best result for all types of datasets. For example, sometimes the estimated spatial noise is too large, which results in an overly-conservative estimation of spatial footprints. Hence, we have introduced a sparseness penalty on top of the estimated scaling factor for the  $\ell_1$ -norm term. This parameter gives users more control over how sparsity should be weighted in the updating process. The higher the number, the higher the penalty imposed by the  $\ell_1$ -norm, and the more sparse the spatial footprints will become. The effect of this parameter can be visualized with the tool shown in Figure 10. Users can employ this tool to determine the best sparseness penalty for their data, where the binarized spatial footprint representing non-zero terms should approach the visible part of the spatial footprint as much as possible, without reducing the amplitude of spatial footprints to the extent that cells are discarded in the spatial update. Figure 11 shows an example of the effect of changing the sparseness penalty on the resulting spatial footprints. A sparseness penalty of 0.1 is considered appropriate in this case. When the sparseness penalty is set much lower, many of the additional 'fragments' begin to appear in the binarized spatial footprint, even if they are not part of the cell. On the other hand, when the sparseness penalty is set too high, some cells are discarded. In the interactive visualization tool, users can inspect the temporal dynamics of these discarded cells. In general, however, we do not recommend exploiting the sparseness penalty during the spatial update to filter cells since this step does not have an explicit model of the temporal signal and thus has no power to differentiate real cells from noise.

In addition, a dilation window parameter must be specified by the user. To reduce the amount of computation when calculating how each pixel weighs onto each cell, we only update weights for cells that are close to each pixel. For each cell, an ROI is computed by performing a morphological dilation process on the previous spatial footprints of that cell. If a pixel lies outside of a cell's region of interest, this cell will not be considered when updating the pixel's weight. Thus, the dilation window parameter determines the maximum distance a cell is allowed to grow during the update compared to its previous spatial footprints. This parameter should be set large enough so that it does not interfere with the spatial update process, but at the same time not so large as to impact performance. The expected cell diameter in pixels is a good starting point.

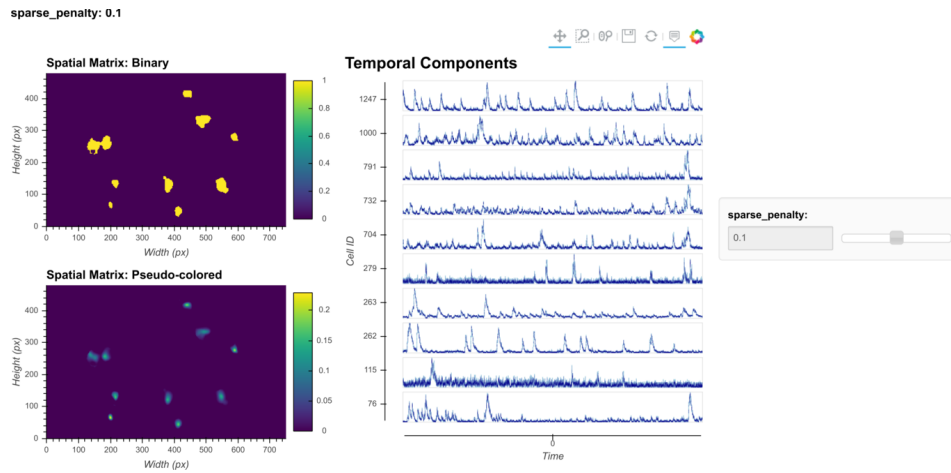


**Figure 10: Visualization of spatial updates.** Here 10 cells are randomly chosen to pass through spatial update with different parameters. The resulting spatial footprints, as well as binarized footprints, are plotted. In addition, the corresponding temporal traces of cells are plotted. The user can visually inspect the size and shape of the spatial footprints and at the same time easily determine whether the results are sparse enough by looking at the binarized footprints.

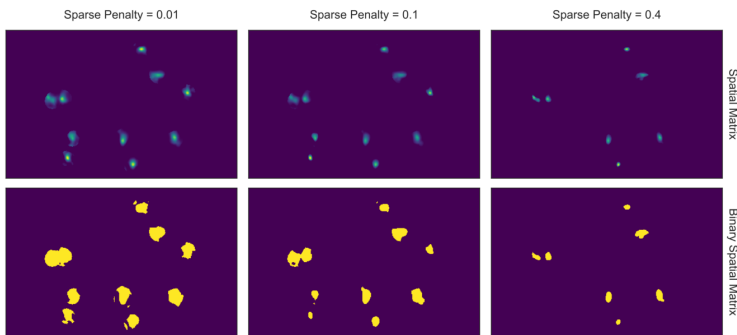


**Figure 11: Effect of sparseness penalty in spatial update.** Here the sum projection of the spatial matrix and binarized spatial matrix are shown for 3 different sparse penalties. A sparseness penalty of 0.1 is considered appropriate in this case. When the sparseness penalty is set lower, artifacts begin to appear. On the other hand, when the sparseness penalty is set higher, cells are dropped out.

### Temporal update

Next, we proceed to the temporal update of the CNMF algorithm. Please refer to the original paper for the detailed derivation [35]. Here, given the spatial matrix and background terms, we update the temporal matrix so that it best fits the input data ( $\mathbf{Y}$ ). First, we subtract the background term from the input data, leaving only the noisy signal from cells. We then project the data onto the spatial footprints of cells, taking into account the overlaps between cells. This process results in a two-dimensional matrix representing the raw temporal activity of each cell.

The CNMF algorithm models the relationship between the underlying ‘spiking’ and the calcium dynamics of a cell as an auto-regressive (AR) process. It should be noted that although the underlying process that drives calcium influx is presumably the actual firing of cells, the ‘spiking’ signal is modeled as a continuous variable instead of a binary variable, and strictly speaking, it is only a de-convolved calcium signal. Following convention, we will refer to this variable as ‘spike signal’, which is an approximation of the underlying cellular activity that drives calcium influx. But it should be understood that the exact relationship between this variable and the actual firing rate of cells is unclear, since the absolute amount of fluorescence generated by a single spike, as well as the numerical effect of integrating multiple spikes on the resulting calcium signal, is unknown.

We first estimate the coefficients for the AR model. The coefficients of the AR model can be conveniently estimated from the autocorrelation of the estimated temporal activity. In addition, noise power for each cell is also estimated directly from the signal. In practice, we find that during the estimation of the AR model parameters, it is helpful to first smooth the signal, otherwise the time constant of the AR model tends to be biased by high frequency noise. Users should again use the peak-to-noise-refinement cut-off frequency for both estimation of the noise power and smoothing of the signals. Finally, we update the temporal matrix by minimizing a target function for different cells, similar to what was done with the spatial matrix. Again, the target function contains an error term and a  $\ell_1$ -norm term. We also introduce a sparseness penalty parameter to control the balance between the two terms. The error term contains the difference between input signal and estimated calcium dynamics, while the  $\ell_1$ -norm term regulates the sparsity of the “spiking” signal. Pre-estimated AR coefficients allow for a determined relationship between the ‘spiking’ signal and calcium dynamics for a given cell. Thus, the problem can be transformed and simplified as minimizing the target function over ‘spiking’ signals of different cells.

In practice, it is computationally more efficient to break down the minimization problem into smaller pieces and update subsets of cells independently and in parallel. To do so, we first identify non-overlapping cells using a Jaccard index, which measures the amount of overlap between the spatial footprints of different cells. Once we identify these individual cells, we can update them independently so that an optimization problem and target function are formulated for each cell independently. Here, we set a cutoff Jaccard index where cells above this amount of overlap are updated in parallel. During the updating process, two additional terms are introduced: a baseline term to account for constitutive non-zero activity of cells and an initial calcium concentration to account for a ‘spiking’ that started just prior to recording. The initial calcium concentration term is a scalar that is recursively multiplied by the same AR coefficient estimated for the cell. The resulting time trace, modeling the decay process of a ‘spiking’ event prior to the recording, is added on top of the calcium trace. The baseline activity term is also a scalar that is simply added on top of all the modeled signals. Both terms are often zero, but they are nevertheless saved and visualized. The  $\ell_1$ -norm in the optimization problem is known to reduce not only the number of non-zero terms (i.e., promotes sparsity), but also the amplitude/value of non-zero terms. This effect is unwanted, since in some cases the numerical value of the resulting ‘spike’ signal can become too small as a side-effect of promoting sparsity, making it hard to interpret and compare the ‘spike’ signal for downstream analysis. To counteract this phenomenon, we introduce a *post hoc* scaling process. After the temporal

update, each cell is assigned a scaling factor to scale all the fitted signals to the appropriate values. The scaling factor is solved by least square minimizing the error between the fitted calcium signal and the projected raw signal.

The critical parameters in temporal updates are as follows: (1) The order of the AR model, which is usually 1 or 2. Users should choose 1 if near-instantaneous rise time is presented in the calcium dynamics of the input data (*i.e.*, from the relatively slow sampling rate) and should choose 2 otherwise; (2) the cut-off frequency for noise used for both noise power estimation and pre-smoothing of the data during AR coefficients estimation. Users should use the values set during peak-to-noise ratio refinement; (3) the threshold for the Jaccard index determining which cells can be updated independently. Users should use a value as low as possible, as long as the speed of this step is acceptable (with large amounts of cells packed closely together, a low threshold may dramatically slow down this step), or visually inspect how sparse the spatial footprints are and determine what amount of overlap between spatial footprints results in significant crosstalk between cells; (4) The sparseness penalty is best set through visualization tools. The effect of any parameter on the temporal update can be visualized through the tool shown in Figure 12, where the result of the temporal update for 10 randomly selected cells are plotted as traces. There are a total of 4 traces shown for each cell: the calcium signal, the deconvolved ‘spiking’ signal, the projected raw signal, and the ‘fitted signal’. The ‘fitted signal’ is very similar to the calcium signal and is often indistinguishable from the later. The difference between them is that the ‘fitted signal’ also includes the baseline term and the initial calcium concentration term. Hence, the ‘fitted signal’ should better follow the projected raw signal, but it may be less interesting for downstream analysis. Toggling between different parameters triggers the dynamic update of the plots, helping the user to determine the best parameters for their data. Additionally, we highlight the effect of the sparseness penalty on resulting fitted calcium signals and spike signals in Figure 13. The effect is most evident in the ‘fitted spikes’ trace, which corresponds to the spike signal and can arguably be interpreted as a measure of the underlying neural activity per frame scaled by an unknown scalar. Here, a sparseness penalty of 1 is considered most appropriate. A lower sparseness penalty will introduce many false positive signals which do not correspond to real calcium dynamics, as can be seen in the plots. On the other hand, too high a sparseness penalty will produce false negatives where clear rises in the raw signal are not accompanied by spikes.

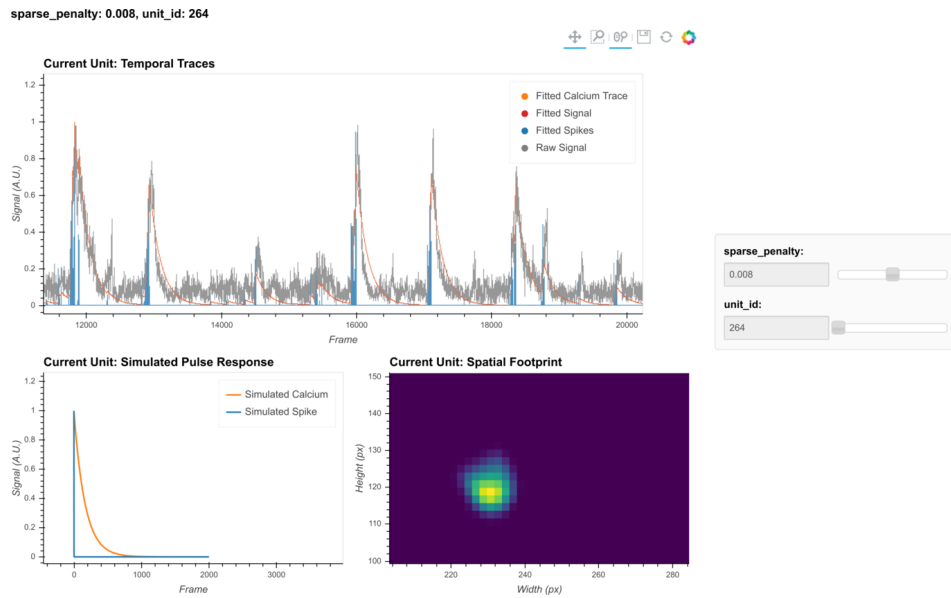


**Figure 12: Visualization of temporal update.** Here, a subset of cells is randomly chosen to pass through temporal updates with different parameters. The raw signal, the fitted signal, the fitted calcium traces, and the spike signals are overlaid in the same plot. In addition, a simulated pulse-response based on the estimated auto-regressive parameters is plotted with the same time scale. Furthermore, the corresponding spatial footprint of the cell is plotted for cross-reference. With a given set of parameters, the user can visually inspect whether the pulse-response captures the typical calcium dynamics of the cell, and whether the timing and sparsity of the spike signal fit well with the raw data.

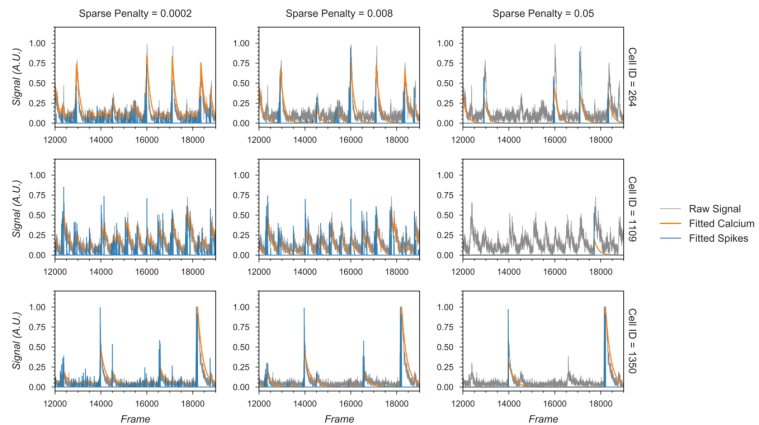


**Figure 13: Effect of the sparseness penalty in temporal update.** Here, 3 example cells are selected and passed to the temporal update with different sparseness penalties. The “Raw Signal” corresponds to the input video projected onto predetermined spatial footprints. The “Fitted Signal” and “Fitted Spikes” correspond to the resulting model-fitted calcium dynamics and spike signals. A sparseness penalty of 1 (middle column) is considered appropriate in this case.

## Merging cells

The CNMF algorithm can sometimes misclassify a single cell as multiple cells. To counteract this phenomenon, we implement a step to merge cells based on their proximity and temporal activity. All cells with spatial footprints sharing at least one pixel are considered candidates for merging, and the pair-wise correlation of their temporal activity is computed. Users can then specify a threshold where cell pairs with activity correlations above the threshold are merged. Merging is done by taking the sum of the respective spatial footprints and the mean of all of the temporal traces for all cells to be merged. Since this is only a simple way to correct for the number of estimated cells and does not fit numerically with what the model CNMF assumes, merging is only done between iterations of CNMF, but not at the end.

## *Cross registration*

After completing the analysis of individual recording sessions, users can register cells across sessions. While more complex approaches are proposed in other pipelines [15,16], here, our intention is simplicity. To account for shifts in the field of view from one session to the next, we first align the field of view from each session based upon a summary frame. Users can either choose a max projection of each pre-processed and motion-corrected video, or a summed projection of the spatial footprints of all of the cells. Users can also choose which session should be used as the template for registration, to which every other session should be aligned. We use a standard cross-correlation based on a template-matching algorithm to estimate the translational shifts for each session relative to the template and then correct for this shift. The weighted centroid of each cell's spatial footprint is then calculated and pair-wise centroid distances are used to cross-register cells. A distance threshold (maximum pixel distance) is set. Users should choose this threshold carefully to reflect the maximum expected displacement of cells across sessions after registration. We found that a threshold of 5 pixels works well. Finally, a pair of cells must be the closest cells to each other in order to be considered the same cell across sessions.

To extend this method to more than two sessions, we first cross-register all possible session pairs. We then take the union of all these pair-wise results and transitively extend the cross-registration across more than two sessions. At the same time, we discard all matches that result in conflicts. For example, if cell A in the first session is matched with cell B in the second session, and cell B is in turn matched with cell C in the third session, but cells A and C are not matched when directly registering the first and third sessions, all of these matches are discarded and all three cells are treated as individual cells. We recognize that this approach might be overly conservative. However, we believe that this strategy provides an easy-to-interpret result that does not require users to make decisions about whether to accept cell pairs that could conflict across sessions.

To save computation time, we implement a moving window where centroid distances are only calculated for cell pairs within these windows. Users should set the size of windows to be much larger than the expected size of cells.

### *Hardware and dependencies*

Minian has been tested using OSX, Linux, and Windows operating systems. Additionally, although we routinely use Minian on specialized analysis computers, the pipeline works on personal laptops for many standard length miniature microscope experiments. Specifications of all of the computers that have been tested can be found in Tested hardware specifications. We anticipate that any computer with at least 16GB of memory will be capable of processing at least 20 minutes of recording data, although increased memory and CPU power will speed up processing. Moreover, due to the read-write processes involved in out-of-core computation, we recommend that the videos to be processed are held locally at the time of analysis, preferably on a solid-state drive. The relatively slow speed of transfer via ethernet cables, Wi-Fi, or USB cables to external drives will severely impair analysis times.

Minian is built on top of project Jupyter [38], and depends heavily on packages provided by the open-source community, including numpy [39], scipy [40], xarray [41], holoviews [42], bokeh [43], opencv [44], and dask [45]. A complete list of direct dependencies for Minian can be found in List of dependencies. Of note, the provided install instructions handle the installation of all dependencies.

## **Results**

To validate Minian, we looked at the spatial footprints and spike signals from Minian's CNMF output and compared them to the preprocessed data to see if they produced expected results across two brain regions, hippocampal CA1 and the nucleus accumbens (Figure 14).

Specifically, we began by validating spatial footprints. We computed a maximum projection across all frames in the preprocessed video and compared them with all the spatial footprints of detected cells. We saw that the spatial footprints correlated well with the max projection. To quantify this result, we calculated the correlation between the max projection image and the summed projection of spatial footprints across all cells. Then, we generated a null distribution of this correlation value by shuffling the location of each cell randomly 1000 times and calculating the correlation between the max projection and shuffled spatial footprints. We found that the observed correlation is significant compared to the correlations from the shuffled footprints ( $p < 0.001$ ). Our results indicate that Minian is able to extract cell locations that match the expected locations based on the maximum projection.

Finally, we validated the spike signal by inspecting whether they captured meaningful calcium dynamics. We first projected the preprocessed video onto the spatial footprint of each cell to get a preprocessed signal for each cell. Since the spike signals tend to be noisy, we binarized the spike signal by fitting a Gaussian-mixture model. We assumed that larger values in the spike signals corresponded to real calcium events, and that all other values that fell into a Gaussian distribution with lower mean were set to zero. We then aligned the preprocessed signals to the onset of all the calcium events and inspected the mean across all cells. We found that on average the aligned preprocessed signals show a waveform that is similar to the expected calcium dynamics. In contrast, when we randomly shuffled the timing of the spike signals independently for each cell and aligned the shuffled preprocessed signal to the shuffled "calcium events", the waveform completely vanished. Taken together, these validations confirm

that Minian is indeed capable of detecting both the location of cells and the calcium activities for each cell.

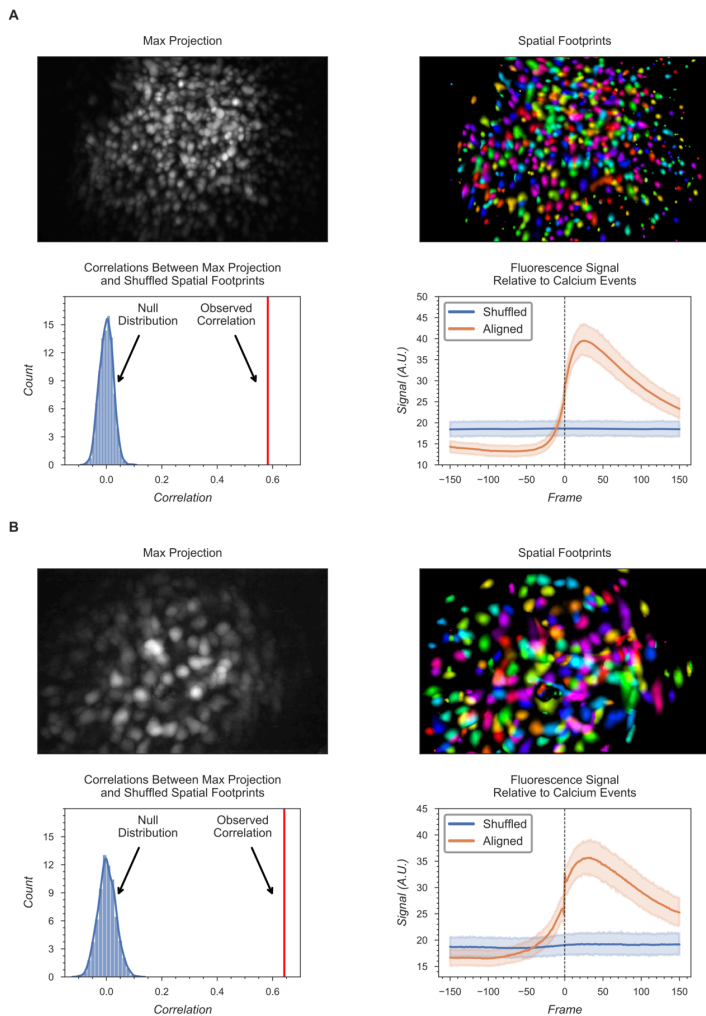


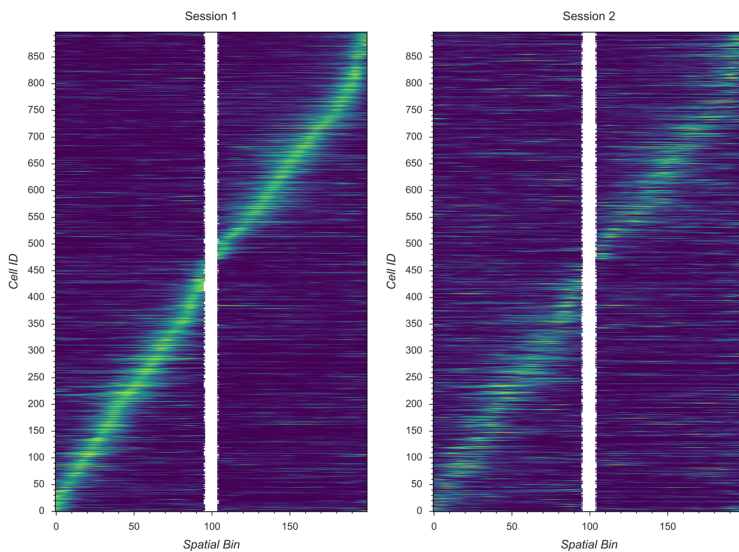
**Figure 14: Validation of Minian in hippocampal CA1 (A) and nucleus accumbens (B).** The spatial footprints and spike signals are validated against preprocessed data. For both brain regions, the max projection of preprocessed video and pseudo-colored spatial footprints are plotted. These plots reveal that the spatial footprints of detected cells match with the max projection, where presumably all cells can be seen. To quantify this result, we calculate the correlation between the max projection image and the sum projection of spatial footprints of all cells. Then, a null distribution of the correlation value is generated by shuffling the location of cells. Both the observed correlation and the null distribution are summarized in a single plot showing that the observed correlation is significant ( $p < 0.001$ ). Finally, the spike signal is validated against signals extracted from preprocessed data. The preprocessed signal is either aligned to the onset of each binarized spike signal or shuffled. The resulting averaged preprocessed signal is plotted with a 95% confidence interval. The onset of the binarized spike signal is shown as frame 0 and marked with a dashed line. We observe that on average the onset of a binarized spike signal captured calcium dynamics similar to what would be expected, and which completely vanished in the shuffled data.

In addition to direct validation of the output for single session, we wanted to validate the scientific significance of the spike signal, as well as the quality of the cross-session registration, and ensure that Minian is capable of generating meaningful results consistent with the existing literature. We leveraged the extensively documented properties of place cells in rodent hippocampal CA1 [46]. Place cells have been shown to have consistent place fields across at least two days [32,47] with only a minority of detected cells undergoing place field remapping. Here, we looked at place field stability across two linear track sessions (Figure 15 A). Briefly, animals were trained to run back and forth on a 2 m linear track while wearing a Miniscope to obtain water rewards available at either end [48]. The time gap between each session was 2 days. Calcium imaging data were analyzed with Minian, while the location of animals was extracted with an open-source behavioral analysis pipeline ezTrack [17]. The resulting calcium dynamics and animal behavior were aligned with the timestamps recorded by Miniscope data acquisition software (miniscope.org). We used the spike signal for our downstream analysis. To calculate average spatial activity rate, we binned the 2-meters long track into 100 spatial bins. In addition, we separated the epochs when the animals are running in opposite directions, resulting in a total of 200 spatial bins. We then smoothed both the binned activity rate and animal's occupancy with a Gaussian kernel with a standard deviation of 5 cm. We classified place cells based on three criteria: a spatial information criterion, a stability criterion, and a place field size criterion [48]. (See Classification of place cells for more detail.) Finally, we analyzed cells that are cross-registered by Minian and are classified as place cells in both sessions. We then calculated the Pearson correlation for the average spatial firing rate for each cross-registered cell. We found that, on average, place cells have a correlation of ~0.6, which is consistent with the existing literature [48].

Next, we validated the cross-session registration to verify that the correct cells were being matched across days. We translated the spatial footprints of the second session in both directions up to 50 pixels and registered the cells with the shifted spatial footprints. We then carried out the same analysis with the registration results from shifted spatial footprints. We found that the average correlations between spatial firing patterns have higher values when the shifts are close to zero (Figure 15 B).

In conclusion, Minian can reliably process *in vivo* calcium imaging data and produce results that are in agreement with the known properties of rodent CA1. Minian can thus help neuroscience labs easily implement and select the best parameters for their calcium analysis pipeline by providing detailed instructions and visualizations.

A



B

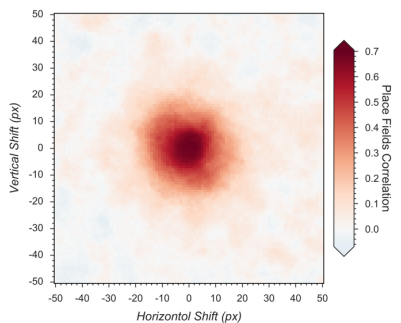


**Figure 15: Validation of Minian with hippocampal CA1 place cells.** (A) Matching place cells from two recording sessions. In both sessions, animals run on a 2-meter-long linear track with water reward at both ends. The track is divided into 200 spatial bins. The mean “firing” rate calculated from the spike signal for each cell is shown. Cell IDs are assigned by Minian when each session is analyzed independently. (B) Averaged correlations of spatial firing rates with different artificial shifts. We artificially shifted the spatial footprints of the second linear track session, then carried out registration and calculated a mean correlation of spatial firing rates for all place cells. The artificial shifts were relative to the aligned spatial footprints and range from -50 to 50 pixels.

## Discussion

### Making open science more accessible

Neuroscience has benefitted tremendously from open-source projects, ranging from DIY hardware [1] to sophisticated algorithms [2]. Open-source projects are impactful because they make cutting-edge technologies available to neuroscience labs with limited resources, as well as opening the door for innovation on top of previously established methods. We believe that openly sharing knowledge and tools is just the first step. Making knowledge accessible even to non-experts should one of the ultimate goals of open-source projects.

With the increasing popularity of miniaturized microscopes [33], there has been significant interest in analysis pipelines that can reliably extract neural activities from the data. Numerous algorithms have been developed to solve this problem [10,12,14,18,19,35], and many of them are implemented as open-source packages that can function as a one-stop pipeline [11,13,15]. However, one of the biggest obstacles for neuroscience labs in adopting analysis pipelines is the difficulty in understanding the exact operation of the algorithms, leading to two notable challenges: First, researchers face difficulties adjusting the parameters when the data they have collected are out of the expected scope of the pipeline's default parameters. Second, even after neural activity data is obtained, it is hard for researchers to be sure that they have chosen the best approaches and parameters for their dataset. Indeed, it has been found that depending on the features of the data and the metric used, more sophisticated algorithms do not always outperform simpler algorithms [49], making it even harder for researchers to interpret the results obtained from some analysis pipelines. Researchers therefore often have to outsource data analysis to experts with strong computational backgrounds or simply trust the output of the algorithms being used. Minian was created to address these challenges. By providing not only detailed documentation of all functions, but also by providing rich interactive visualizations, Minian helps researchers to develop an intuitive understanding of the operations of algorithms without expertise in mathematics or computer science. These insights help researchers choose the best parameters, as well as to become more confident in their interpretation of results. Furthermore, transparency regarding the underlying algorithms enables researchers to develop in-house modifications of the pipeline, which is a common practice in neuroscience labs. We believe that Minian will contribute to the open science community by making the analysis of calcium imaging data more accessible and understandable to neuroscience labs.

### *Limitations*

Although Minian provides users with insights into the parameter tuning process across different brain regions, these insights are achieved mainly through visual inspection. Ultimately, however, the performance of an analysis pipeline should be measured objectively. Although calcium imaging has been validated with electrophysiology under *ex vivo* settings [50], ground-truth data for single-photon *in vivo* calcium imaging are lacking, making objective evaluation of the algorithms difficult. Therefore, here we have provided only indirect validations of the pipeline by recapitulating well-established biological findings.

### **Supplemental information**

#### *Parallel and out-of-core computation with dask*

In Minian, we use a modern parallel computing library called dask to implement parallel and out-of-core computation. Dask divides the data into small chunks along all dimensions, then flexibly merges the data along some dimensions in each step. We leverage the fact that each step in our pipeline has at least one dimension where each slice on that dimension can be processed independently, thus requiring no interpolation or special handling of borders when merged together which produces results as if no chunking had been done. Consequently, our pipeline fully supports out-of-core computation, and memory demand is dramatically reduced. In practice, a modern laptop can easily handle the analysis of a full experiment with a typical recording length of up to 20 minutes. Dask also enables us to carry out lazy evaluation of many

steps where the computation is postponed until the result is needed, for example, when a plot of the result is requested. This enables selective evaluation of operations only on the subset of data that will become part of the visualization and thus helps users to quickly explore a large space of parameters without committing to the full operation each time.

#### *Seeds refinement with a Gaussian-Mixture-Model*

As described in the main text, an alternative strategy to thresholding fluorescence intensity during seeds initialization is to explicitly model the distribution of fluorescence fluctuations of all candidate seeds and select those with relatively higher fluctuation. Here, we describe this process and the rationale. Since the seeds are generated from local maxima, they include noise from relatively empty regions with no actual cells. The seeds from these regions usually have low fluctuations in fluorescence across time and can be classified as spurious. To identify these cases, we compute a range of fluctuation for each seed (range of min-max across time), and model these ranges with a Gaussian-Mixture-Model of two components. The fluctuations from 'noise' seeds compose a Gaussian distribution with low fluctuation, while seeds from actual cells assume a higher degree of fluctuation and form another Gaussian distribution with a higher mean. Any seed whose fluctuations belong to the lower Gaussian distribution is discarded in this step. To compute the range of fluctuation for each seed, we compute the difference between the 99.9 and 0.1 percentile of all fluorescence values across time, which is less biased by outliers than the actual maximum and minimum values.

Normally, this step is parameter-free. In rare cases, there are regions containing noise while other regions are almost completely dark. Thus, seeds from these two regions will form two peaks in the distribution of what the user would consider 'bad seeds', and a Gaussian-Mixture-Model with two components will no longer be valid. In such cases users can tweak the number of components (number of modeled Gaussian distributions), as well as the number of components to be considered as composed of real signal. However, because the two noise distributions are likely to overlap to some degree, using two components will likely suffice. The distribution of fluctuations, the Gaussian-Mixture-Model fit, and the resulting seeds, are visualized, enabling the user to judge the appropriateness and accuracy of this step. It should be noted that in practice, we have found this process to depend heavily on the relative proportion of the 'good' and 'bad' seeds and can easily result in a significant amount of false negatives if the proportion of the 'bad' seed is too low. This makes the Gaussian-Mixture-Model approach less stable and in general less preferable to simple thresholding unless a good threshold of fluorescence intensity cannot be easily determined.

#### *Classification of place cells*

We use the spatially-binned averaged 'firing' rate calculated from binarized spike signals to classify whether each cell is a place cell. A place cell must simultaneously satisfy three criteria: a spatial information criterion, a stability criterion, and a place field size criterion. For the spatial information criterion, we use the joint information between 'firing' rate and an animal's location measured in bits per 'spike'. A cell must have significantly high (see below) spatial information to pass the spatial information criterion. For the stability criterion, we calculate the Fisher z-transformation of the Pearson correlation coefficient between spatial 'firing' patterns across different trials within a recording session. A trial is defined as the time which the animal runs

from one end of the linear track to the other and returns to the starting location. We calculate the z-transformed correlation between the odd number of trials and the even number of trials, as well as between the first half of the trials and the second half of the trials. We then average these two measures of correlations and use that as the measure of stability for a cell. Again, a cell must have significantly high (see below) stability to pass the stability criterion. For the place field size criterion, we define the place field of each cell as the longest contiguous spatial bin where the averaged ‘firing’ rate exceeded the 95th percentile of all averaged firing rate bins. A cell must have a place field larger than 4 cm (*i.e.* 2 spatial bins) to pass the place field size criterion. To define significance for both the spatial information criterion and the stability criterion, we obtain a null distribution of the measurements (spatial information and stability) with a bootstrap strategy, where we roll the timing of activities by a random amount for each cell 1000 times. The true measurement is defined as significant if it exceeds the 95th percentile of its null distribution ( $p < 0.05$ ).

#### *Tested hardware specifications*

The hardware specifications of computers that have effectively run Minian are summarized in the table below.

**Table 1: A list of computers tested with Minian with specifications.** Listed roughly by increasing computation power.

Manufacture	Model	CPU	RAM	Storage	Operating System
Microsoft	Surface Pro 6	Intel Core i5-8250U 1.6GHz x 4	8GB	256GB SSD	Windows 10
Dell	Precision 5530	Intel Core i5-8400H 2.5GHz x 4	16GB	256GB SSD	Ubuntu 18.04
Apple	MacBook Pro 152	Intel Core i7-8559U 2.7GHz x 4	16GB	1TB SSD	macOS 10.14 Mojave
custom-built	custom-built	Intel Xeon E5-1650 3.6GHz x 6	128GB	6TB HDD	Ubuntu 17.1

#### *List of dependencies*

**Table 2: A list of open-source packages and the specific versions on which Minian depends.**

Package	Version
av	7.0
bokeh	1.4
bottleneck	1.3
cairo	1.16
cvxpy	1.0

dask	2.11
datashader	0.1
distributed	2.11
ecos	2.0
ffmpeg	4.1
fftw	3.3
holoviews	1.12
ipython	7.12
ipywidgets	7.5
jupyter	1.0
matplotlib	3.1
natsort	7.0
netcdf4	1.5
networkx	2.4
nodejs	13.9
numba	0.48
numpy	1.18
opencv	4.2
pandas	1.0
panel	0.8
papermill	2.0
param	1.9
pip	20.0
pyfftw	0.12
python	3.8
scipy	1.4
scs	2.1
statsmodels	0.11
tifffile	2020.2
tqdm	4.43
xarray	0.15
zarr	2.4
medpy	0.4
simpleitk	1.2

## Conflict of interest

The authors declare that they have no competing financial interests.

## Funding

*NIH F32AG067640*

- William Mau

*NIH BRAIN Initiative (R01 EB028166)*

- Kanaka Rajan

*James S. McDonnell Foundation's Understanding Human Cognition Scholar Award*

- Kanaka Rajan

*NSF FOUNDATIONS Award (NSF1926800)*

- Kanaka Rajan

*CURE Epilepsy Taking Flight Award*

- Tristan Shuman

*American Epilepsy Society Junior investigator Award*

- Tristan Shuman

*R03 NS111493*

- Tristan Shuman

*R21 DA049568*

- Tristan Shuman

*R01 NS116357*

- Tristan Shuman

*U01 NS094286-01*

- Daniel Aharoni

*1700408 Neurotech Hub*

- Daniel Aharoni

*NIH DP2MH122399*

- Denise J. Cai

*R01 MH120162*

- Denise J. Cai

*Botanical Center Pilot Award from P50 AT008661-01 from the NCCIH and the ODS (Pasinetti PI)*

- Denise J. Cai

*One Mind Otsuka Rising Star Award*

- Denise J. Cai

*McKnight Memory and Cognitive Disorders Award*

- Denise J. Cai

*Klingensteins-Simons Fellowship Award in Neuroscience*

- Denise J. Cai

*Mount Sinai Distinguished Scholar Award*

- Denise J. Cai

*Brain Research Foundation Award*

- Denise J. Cai

*NARSAD Young Investigator Award*

- Denise J. Cai

## **Acknowledgements**

We thank Eftychios A Pnevmatikakis, Andrea Giovannucci, and Liam Paninski for establishing the theoretical foundation and providing helpful insight for the pipeline. We thank Giovanni Idili, Zoran Sinnema, Dan Knudsen, and Paolo Bazzigaluppi for contributing to the documentation and continuous integration of the pipeline. We thank Brandon Wei, Mimi La-Vu, and Christopher Lee for contributing to the dataset used in Minian development and testing. The authors acknowledge support from following funding sources: WM is supported by NIH F32AG067640. KR is supported by NIH BRAIN Initiative (R01 EB028166), James S. McDonnell Foundation's Understanding Human Cognition Scholar Award, and NSF FOUNDATIONS Award (NSF1926800). TS is supported by CURE Epilepsy Taking Flight Award, American Epilepsy Society Junior investigator Award, R03 NS111493, R21 DA049568, and R01 NS116357. DA is

supported by U01 NS094286-01, and 1700408 Neurotech Hub. DJC is supported by NIH DP2MH122399, R01 MH120162, Botanical Center Pilot Award from P50 AT008661-01 from the NCCIH and the ODS (Pasinetti PI), One Mind Otsuka Rising Star Award, McKnight Memory and Cognitive Disorders Award, Klingenstein-Simons Fellowship Award in Neuroscience, Mount Sinai Distinguished Scholar Award, Brain Research Foundation Award, and NARSAD Young Investigator Award.

## References

### 1. The Future Is Open: Open-Source Tools for Behavioral Neuroscience Research

Samantha R. White, Linda M. Amarante, Alexxai V. Kravitz, Mark Laubach  
*eneuro* (2019-07) <https://doi.org/ggcmcv>  
DOI: 10.1523/eneuro.0223-19.2019 · PMID: 31358510 · PMCID: PMC6712209

### 2. Open source tools for large-scale neuroscience

Jeremy Freeman  
*Current Opinion in Neurobiology* (2015-06) <https://doi.org/ghqn37>  
DOI: 10.1016/j.conb.2015.04.002 · PMID: 25982977

### 3. Open source modules for tracking animal behavior and closed-loop stimulation based on Open Ephys and Bonsai

Alessio Paolo Buccino, Mikkel Elle Lepperød, Svenn-Arne Dragly, Philipp Häfliger, Marianne Fyhn, Torkel Hafting  
*Journal of Neural Engineering* (2018-10-01) <https://doi.org/ggp3mh>  
DOI: 10.1088/1741-2552/aacf45 · PMID: 29946057

### 4. An open source automated two-bottle choice test apparatus for rats

Jude A. Frie, Jibran Y. Khokhar  
*HardwareX* (2019-04) <https://doi.org/ghr3cd>  
DOI: 10.1016/j.ohx.2019.e00061 · PMID: 31245655 · PMCID: PMC6594565

### 5. Bonsai: an event-based framework for processing and controlling data streams

Gonçalo Lopes, Niccolò Bonacchi, João Frazão, Joana P. Neto, Bassam V. Atallah, Sofia Soares, Luís Moreira, Sara Matias, Pavel M. Itskov, Patrícia A. Correia, ... Adam R. Kampff  
*Frontiers in Neuroinformatics* (2015-04-08) <https://doi.org/ggbj87>  
DOI: 10.3389/fninf.2015.00007 · PMID: 25904861 · PMCID: PMC4389726

### 6. Feeding Experimentation Device (FED): A flexible open-source device for measuring feeding behavior

Katrina P. Nguyen, Timothy J. O'Neal, Olurotimi A. Bolonduro, Elecia White, Alexxai V. Kravitz  
*Journal of Neuroscience Methods* (2016-07) <https://doi.org/f8rcmm>  
DOI: 10.1016/j.jneumeth.2016.04.003 · PMID: 27060385 · PMCID: PMC4884551

### 7. JAABA: interactive machine learning for automatic annotation of animal behavior

Mayank Kabra, Alice A Robie, Marta Rivera-Alba, Steven Branson, Kristin Branson  
*Nature Methods* (2013-01-01) <https://doi.org/gg66kh>  
DOI: 10.1038/nmeth.2281 · PMID: 23202433

**8. DeepLabCut: markerless pose estimation of user-defined body parts with deep learning**

Alexander Mathis, Pranav Mamtanna, Kevin M. Cury, Taiga Abe, Venkatesh N. Murthy, Mackenzie Weygandt Mathis, Matthias Bethge

*Nature Neuroscience* (2018-08-20) <https://doi.org/gd249k>

DOI: 10.1038/s41593-018-0209-y · PMID: 30127430

**9. Automated classification of self-grooming in mice using open-source software**

Bastijn J. G. van den Boom, Pavlina Pavlidi, Casper J. H. Wolf, Adriana H. Mooij, Ingo Willuhn

*Journal of Neuroscience Methods* (2017-09) <https://doi.org/gb2wxk>

DOI: 10.1016/j.jneumeth.2017.05.026 · PMID: 28648717

**10. Efficient and accurate extraction of in vivo calcium signals from microendoscopic video data**

Pengcheng Zhou, Shanna L Resendez, Jose Rodriguez-Romaguera, Jessica C Jimenez, Shay Q Neufeld, Andrea Giovannucci, Johannes Friedrich, Eftychios A Pnevmatikakis, Garret D Stuber, Rene Hen, ... Liam Paninski

*eLife* (2018-02-22) <https://doi.org/gfxbdp>

DOI: 10.7554/elife.28728 · PMID: 29469809 · PMCID: PMC5871355

**11. MIN1PIPE: A Miniscope 1-Photon-Based Calcium Imaging Signal Extraction Pipeline**

Jinghao Lu, Chunyuan Li, Jonnathan Singh-Alvarado, Zhe Charles Zhou, Flavio Fröhlich, Richard Mooney, Fan Wang

*Cell Reports* (2018-06) <https://doi.org/gdpc2z>

DOI: 10.1016/j.celrep.2018.05.062 · PMID: 29925007 · PMCID: PMC6084484

**12. Automated Analysis of Cellular Signals from Large-Scale Calcium Imaging Data**

Eran A. Mukamel, Axel Nimmerjahn, Mark J. Schnitzer

*Neuron* (2009-09) <https://doi.org/bhwqvc>

DOI: 10.1016/j.neuron.2009.08.009 · PMID: 19778505 · PMCID: PMC3282191

**13. Suite2p: beyond 10,000 neurons with standard two-photon microscopy**

Marius Pachitariu, Carsen Stringer, Mario Dipoppa, Sylvia Schröder, L. Federico Rossi, Henry Dalgleish, Matteo Carandini, Kenneth D. Harris

*Cold Spring Harbor Laboratory* (2017-07-20) <https://doi.org/ggdxxm>

DOI: 10.1101/061507

**14. Fast, Simple Calcium Imaging Segmentation with Fully Convolutional Networks**

Aleksander Klibisz, Derek Rose, Matthew Eicholtz, Jay Blundon, Stanislav Zakharenko

*Lecture Notes in Computer Science* (2017) <https://doi.org/ghm58x>

DOI: 10.1007/978-3-319-67558-9\_33

**15. CalmAn an open source tool for scalable calcium imaging data analysis**

Andrea Giovannucci, Johannes Friedrich, Pat Gunn, Jérémie Kalfon, Brandon L Brown, Sue Ann Koay, Jiannis Taxidis, Farzaneh Najafi, Jeffrey L Gauthier, Pengcheng Zhou, ... Eftychios A Pnevmatikakis

eLife (2019-01-17) <https://doi.org/gf4v82>  
DOI: 10.7554/elife.38173 · PMID: 30652683 · PMCID: PMC6342523

**16. Tracking the Same Neurons across Multiple Days in Ca<sub>2+</sub> Imaging Data**

Liron Sheintuch, Alon Rubin, Noa Brande-Eilat, Nitzan Geva, Noa Sadeh, Or Pinchasof, Yaniv Ziv

*Cell Reports* (2017-10) <https://doi.org/ghdnqz>  
DOI: 10.1016/j.celrep.2017.10.013 · PMID: 29069591 · PMCID: PMC5670033

**17. ezTrack: An open-source video analysis pipeline for the investigation of animal behavior**

Zachary T. Pennington, Zhe Dong, Yu Feng, Lauren M. Vetere, Lucia Page-Harley, Tristan Shuman, Denise J. Cai

*Scientific Reports* (2019-12-27) <https://doi.org/ghm6dp>  
DOI: 10.1038/s41598-019-56408-9 · PMID: 31882950 · PMCID: PMC6934800

**18. Fast online deconvolution of calcium imaging data**

Johannes Friedrich, Pengcheng Zhou, Liam Paninski

*PLOS Computational Biology* (2017-03-14) <https://doi.org/f9tsn9>  
DOI: 10.1371/journal.pcbi.1005423 · PMID: 28291787 · PMCID: PMC5370160

**19. OnACID: Online Analysis of Calcium Imaging Data in Real Time\***

Andrea Giovannucci, Johannes Friedrich, Matt Kaufman, Anne Churchland, Dmitri Chklovskii, Liam Paninski, Eftychios A. Pnevmatikakis

*Cold Spring Harbor Laboratory* (2017-10-02) <https://doi.org/ghqn38>  
DOI: 10.1101/193383

**20. Exact spike train inference via  $\ell_0$  optimization**

Sean Jewell, Daniela Witten

*The Annals of Applied Statistics* (2018-12-01) <https://doi.org/ghm589>  
DOI: 10.1214/18-aoas1162 · PMID: 30627301 · PMCID: PMC6322847

**21. All the light that we can see: a new era in miniaturized microscopy**

Daniel Aharoni, Baljit S. Khakh, Alcino J. Silva, Peyman Golshani

*Nature Methods* (2018-12-20) <https://doi.org/ghdnvz>  
DOI: 10.1038/s41592-018-0266-x · PMID: 30573833

**22. An open-source control system for in vivo fluorescence measurements from deep-brain structures**

Scott F. Owen, Anatol C. Kreitzer

*Journal of Neuroscience Methods* (2019-01) <https://doi.org/ghvk8p>  
DOI: 10.1016/j.jneumeth.2018.10.022 · PMID: 30342106 · PMCID: PMC6258340

**23. Open Ephys: an open-source, plugin-based platform for multichannel electrophysiology**

Joshua H Siegle, Aarón Cuevas López, Yogi A Patel, Kirill Abramov, Shay Ohayon, Jakob Voigts

*Journal of Neural Engineering* (2017-08-01) <https://doi.org/gfvmzq>  
DOI: 10.1088/1741-2552/aa5eea · PMID: 28169219

**24. Open Source Tools for Temporally Controlled Rodent Behavior Suitable for Electrophysiology and Optogenetic Manipulations**

Nicola Solari, Katalin Sviatkó, Tamás Laszlovszky, Panna Hegedüs, Balázs Hangya  
*Frontiers in Systems Neuroscience* (2018-05-15) <https://doi.org/gdns24>  
DOI: 10.3389/fnsys.2018.00018 · PMID: 29867383 · PMCID: PMC5962774

**25. A wireless miniScope for deep brain imaging in freely moving mice**

Giovanni Barbera, Bo Liang, Lifeng Zhang, Yun Li, Da-Ting Lin  
*Journal of Neuroscience Methods* (2019-07) <https://doi.org/ghtkfs>  
DOI: 10.1016/j.jneumeth.2019.05.008 · PMID: 31116963 · PMCID: PMC6636826

**26. A Compact Head-Mounted Endoscope for In Vivo Calcium Imaging in Freely Behaving Mice**

Alexander D. Jacob, Adam I. Ramsaran, Andrew J. Mocle, Lina M. Tran, Chen Yan, Paul W. Frankland, Sheena A. Josselyn  
*Current Protocols in Neuroscience* (2018-07) <https://doi.org/gdr76d>  
DOI: 10.1002/cpns.51 · PMID: 29944206

**27. An open source, wireless capable miniature microscope system**

William A Liberti, L Nathan Perkins, Daniel P Leman, Timothy J Gardner  
*Journal of Neural Engineering* (2017-08-01) <https://doi.org/gf73sj>  
DOI: 10.1088/1741-2552/aa6806 · PMID: 28514229 · PMCID: PMC5955387

**28. NINscope, a versatile miniscope for multi-region circuit investigations**

Andres de Groot, Bastijn JG van den Boom, Romano M van Genderen, Joris Coppens, John van Veldhuijzen, Joop Bos, Hugo Hoedemakers, Mario Negrello, Ingo Willuhn, Chris I De Zeeuw, Tycho M Hoogland  
*eLife* (2020-01-14) <https://doi.org/ghsb8m>  
DOI: 10.7554/elife.49987 · PMID: 31934857 · PMCID: PMC6989121

**29. High-speed volumetric imaging of neuronal activity in freely moving rodents**

Oliver Skocek, Tobias Nöbauer, Lukas Weilguny, Francisca Martínez Traub, Chuying Naomi Xia, Maxim I. Molodtsov, Abhinav Grama, Masahito Yamagata, Daniel Aharoni, David D. Cox, ... Alipasha Vaziri  
*Nature Methods* (2018-05-07) <https://doi.org/gf2n7z>  
DOI: 10.1038/s41592-018-0008-0 · PMID: 29736000 · PMCID: PMC7990085

**30. Imaging Cortical Dynamics in GCaMP Transgenic Rats with a Head-Mounted Widefield Microscope**

Benjamin B. Scott, Stephan Y. Thibierge, Caiying Guo, D. Gowanlock R. Tervo, Carlos D. Brody, Alla Y. Karpova, David W. Tank  
*Neuron* (2018-12) <https://doi.org/gfgk25>  
DOI: 10.1016/j.neuron.2018.09.050 · PMID: 30482694 · PMCID: PMC6283673

### 31. Miniaturized integration of a fluorescence microscope

Kunal K Ghosh, Laurie D Burns, Eric D Cocker, Axel Nimmerjahn, Yaniv Ziv, Abbas El Gamal, Mark J Schnitzer

*Nature Methods* (2011-09-11) <https://doi.org/cv75qh>

DOI: 10.1038/nmeth.1694 · PMID: 21909102 · PMCID: PMC3810311

### 32. Long-term dynamics of CA1 hippocampal place codes

Yaniv Ziv, Laurie D Burns, Eric D Cocker, Elizabeth O Hamel, Kunal K Ghosh, Lacey J Kitch, Abbas El Gamal, Mark J Schnitzer

*Nature Neuroscience* (2013-02-10) <https://doi.org/gdh98h>

DOI: 10.1038/nn.3329 · PMID: 23396101 · PMCID: PMC3784308

### 33. Circuit Investigations With Open-Source Miniaturized Microscopes: Past, Present and Future

Daniel Aharoni, Tycho M. Hoogland

*Frontiers in Cellular Neuroscience* (2019-04-05) <https://doi.org/ghqn39>

DOI: 10.3389/fncel.2019.00141 · PMID: 31024265 · PMCID: PMC6461004

### 34. A shared neural ensemble links distinct contextual memories encoded close in time

Denise J. Cai, Daniel Aharoni, Tristan Shuman, Justin Shobe, Jeremy Biane, Weilin Song, Brandon Wei, Michael Veshkini, Mimi La-Vu, Jerry Lou, ... Alcino J. Silva

*Nature* (2016-05-23) <https://doi.org/f8pp28>

DOI: 10.1038/nature17955 · PMID: 27251287 · PMCID: PMC5063500

### 35. Simultaneous Denoising, Deconvolution, and Demixing of Calcium Imaging Data

Eftychios A. Pnevmatikakis, Daniel Soudry, Yuanjun Gao, Timothy A. Machado, Josh Merel, David Pfau, Thomas Reardon, Yu Mu, Clay Lacefield, Weijian Yang, ... Liam Paninski

*Neuron* (2016-01) <https://doi.org/f8g23x>

DOI: 10.1016/j.neuron.2015.11.037 · PMID: 26774160 · PMCID: PMC4881387

### 36. Fast Nonnegative Deconvolution for Spike Train Inference From Population Calcium Imaging

Joshua T. Vogelstein, Adam M. Packer, Timothy A. Machado, Tanya Sippy, Baktash Babadi, Rafael Yuste, Liam Paninski

*Journal of Neurophysiology* (2010-12) <https://doi.org/fpddqn>

DOI: 10.1152/jn.01073.2009 · PMID: 20554834 · PMCID: PMC3007657

### 37. Template matching techniques in computer vision: theory and practice

Roberto Brunelli

Wiley (2009)

ISBN: 9780470517062

### 38. Jupyter Notebooks – a publishing format for reproducible computational workflows

Thomas Kluyver, Benjamin Ragan-Kelley, Pé, Fernando Rez, Brian Granger, Matthias Bussonnier, Jonathan Frederic, Kyle Kelley, Jessica Hamrick, Jason Grout, ... Jupyter Development Team

*Positioning and Power in Academic Publishing: Players, Agents and Agendas* (2016)

<https://ebooks-iospress.nli/doi/10.3233/978-1-61499-649-1-87>  
DOI: 10.3233/978-1-61499-649-1-87

### 39. Array programming with NumPy

Charles R. Harris, K. Jarrod Millman, Stéfan J. van der Walt, Ralf Gommers, Pauli Virtanen, David Cournapeau, Eric Wieser, Julian Taylor, Sebastian Berg, Nathaniel J. Smith, ... Travis E. Oliphant

*Nature* (2020-09-16) <https://doi.org/ghbfz2>

DOI: 10.1038/s41586-020-2649-2 · PMID: 32939066 · PMCID: PMC7759461

### 40. SciPy 1.0: fundamental algorithms for scientific computing in Python

Pauli Virtanen, Ralf Gommers, Travis E. Oliphant, Matt Haberland, Tyler Reddy, David Cournapeau, Evgeni Burovski, Pearu Peterson, Warren Weckesser, Jonathan Bright, ... SciPy 1.0 Contributors

*Nature Methods* (2020-02-03) <https://doi.org/ggj45f>

DOI: 10.1038/s41592-019-0686-2 · PMID: 32015543 · PMCID: PMC7056644

### 41. xarray: N-D labeled Arrays and Datasets in Python

Stephan Hoyer, Joseph J. Hamman

*Journal of Open Research Software* (2017-04-05) <https://doi.org/gdqdmw>

DOI: 10.5334/jors.148

### 42. holoviz/holoviews: Version 1.13.3

Philipp Rudiger, Jean-Luc Stevens, James A. Bednar, Bas Nijholt,, Andrew, Chris B, Achim Randelhoff, Jon Mease, Vasco Tenner, Maxalbert, ... Kbowen

*Zenodo* (2020-06-23) <https://doi.org/ghm6dq>

DOI: 10.5281/zenodo.3904606

### 43. Bokeh: Python library for interactive visualization

Bokeh Development Team

(2020) <https://bokeh.org/>

### 44. The OpenCV Library

G. Bradski

*Dr. Dobb's Journal of Software Tools* (2000)

### 45. Dask: Library for dynamic task scheduling

Dask Development Team

(2016) <https://dask.org>

### 46. The hippocampus as a spatial map. Preliminary evidence from unit activity in the freely-moving rat

J. O'Keefe, J. Dostrovsky

*Brain Research* (1971-11) <https://doi.org/bwdqcb>

DOI: 10.1016/0006-8993(71)90358-1

**47. Long-term stability of the place-field activity of single units recorded from the dorsal hippocampus of freely behaving rats**

L. T. Thompson, P. J. Best

*Brain Research* (1990-02) <https://doi.org/cp6bjf>

DOI: 10.1016/0006-8993(90)90555-p

**48. Breakdown of spatial coding and interneuron synchronization in epileptic mice**

Tristan Shuman, Daniel Aharoni, Denise J. Cai, Christopher R. Lee, Spyridon Chavlis, Lucia Page-Harley, Lauren M. Vetere, Yu Feng, Chen Yi Yang, Irene Mollinedo-Gajate, ... Peyman Golshani

*Nature Neuroscience* (2020-01-06) <https://doi.org/ghm6dn>

DOI: 10.1038/s41593-019-0559-0 · PMID: 31907437 · PMCID: PMC7259114

**49. Robustness of Spike Deconvolution for Neuronal Calcium Imaging**

Marius Pachitariu, Carsen Stringer, Kenneth D. Harris

*The Journal of Neuroscience* (2018-09-12) <https://doi.org/gd9mcx>

DOI: 10.1523/jneurosci.3339-17.2018 · PMID: 30082416 · PMCID: PMC6136155

**50. Ultrasensitive fluorescent proteins for imaging neuronal activity**

Tsai-Wen Chen, Trevor J. Wardill, Yi Sun, Stefan R. Pulver, Sabine L. Renninger, Amy Baohan, Eric R. Schreiter, Rex A. Kerr, Michael B. Orger, Vivek Jayaraman, ... Douglas S. Kim

*Nature* (2013-07-17) <https://doi.org/gcz68k>

DOI: 10.1038/nature12354 · PMID: 23868258 · PMCID: PMC3777791